Petroleum Science 23 (2026) 4829–4841

Contents lists available at ScienceDirect

Petroleum Science

journal homepage: www.keaipublishing.com/en/journals/petroleum-science

Original Paper

Integrating rock mechanics and optimized mechanical specific energy for real-time pore pressure estimation in high-temperature and high-pressure drilling

Cheng-Kai Weng [a,b], Hong-Wei Yang [a,b,*], Jun Li [a,b,c], Xian-Jun Chen [d], Gong-Hui Liu [a], Shu-Sheng Guo [e], Zhen-Yu Long [a,b], Wang Chen [a,b]

[a] College of Petroleum Engineering, China University of Petroleum (Beijing), Beijing, 102249, China
[b] Hainan Institute of China University of Petroleum (Beijing), Sanya, 572000, Hainan, China
[c] China University of Petroleum-Beijing at Karamay, Karamay, 834000, Xinjiang, China
[d] Hainan Branch of China France Bohai Geoservices Company Limited, Haikou, 570312, Hainan, China
[e] Hainan Branch, CNOOC China Limited, Haikou, 570312, Hainan, China

A R T I C L E I N F O

Article history:
Received 9 June 2025
Received in revised form
25 March 2026
Accepted 26 March 2026
Available online 30 March 2026

Edited by Jia-Jia Fei

Keywords:
Pore pressure
High-temperature and high-pressure well
Mechanical specific energy
Machine learning
Safe drilling

A B S T R A C T

Accurate real-time estimation of pore pressure (*P*p) is essential in high-temperature and high-pressure (HTHP) wells to prevent blowouts and lost circulation, given the complexity of their pressure regimes. However, conventional methods are inadequate: seismic-based and logging-based models are hindered by geological uncertainties, the dc-index principle is incompatible with PDC bits, and reliable while-drilling acoustic measurements remain prohibitively expensive. To overcome existing limitations, a surface-based and real-time *P*p estimation framework is proposed, in which a direct *P*p equation is derived by integrating an approximation using friction-corrected mechanical specific energy as the confined compressive strength (CCS) into the Mohr-Coulomb failure criterion. To ensure high-fidelity inputs for this equation, ridge regression is employed to invert rock strength parameters from drilling data, while a transient thermo-hydraulic model accurately calculates dynamic downhole pressure instead of relying on the static assumption. Validation on five HTHP wells in the Ying-Qiong Basin demonstrates that after accounting for thermo-pressure coupling, the method reduces the mean absolute error (MAE) in *P*p equivalent density by 0.085 g/cm^3 compared to the hydrostatic assumption. Furthermore, the proposed method achieves an MAE of 4.12%, outperforming the dc-index method, which achieves an MAE of 5.78%. Notably, the new method is more stable, with its prediction error envelope remaining within $\pm$5%, whereas the dc-index's error extends to $\pm$10%. Given its theoretical compatibility with modern PDC bits and its demonstrated high accuracy, this surface-based and real-time scheme has the potential to overcome the conventional limitations of *P*p estimation from surface data, providing a robust safeguard for well control in HTHP environments.

1. Introduction

High-temperature and high-pressure (HTHP) wells are characterized by prolonged operational cycles, high drilling costs, and elevated risk (Dabiri et al., 2025; Qin et al., 2023). In addition, formations encountered during drilling commonly exhibit complex and heterogeneous pressure regimes (Chen et al., 2025). Pre-drilling pore pressure (*P*p) forecasts rely on manually interpreted seismic velocities and geological conditions; their accuracy is limited by acquisition errors and subsurface heterogeneity, resulting in large prediction uncertainties that hinder effective drilling design (Li et al., 2019). The risk is particularly pronounced in exploratory wells, where the absence of historical data makes them susceptible to kicks and blowouts during drilling (Ehsan et al., 2025). Real-time formation-pressure monitoring, which estimates bottom-hole *P*p from drilling data, is therefore

* Corresponding author.
E-mail address: zerotone@cup.edu.cn (H.-W. Yang).
Peer review under the responsibility of China University of Petroleum (Beijing).

https://doi.org/10.1016/j.petsci.2026.03.062

fundamental to safe and efficient operations, guiding mud-weight selection and accident prevention (Yang et al., 2005, 2025).

Three principal approaches are available for *P*p estimation: log-based, drilling-performance-based, and seismic-based methods. Hottmann and Johnson (1965) introduced the first log-based technique, Jorden and Shirley (1966) proposed a drilling-performance-based method, and Pennebaker (1968) presented a seismic-based method, which together form the foundation of modern *P*p prediction. Among them, drilling-performance-based estimating relies chiefly on empirical models developed for rotary drilling. Building on the Bingham equation and assuming constant drilling conditions in shale formations, Jorden and Shirley (1966) developed the first rate of penetration (ROP) model, elucidating the relationship between ROP and differential pressure. Their empirical approximations indicated a clear correlation between the model coefficient and differential pressure when parameters other than ROP, weight-on-bit (WOB), and bit type remain constant. On the basis of these findings and the d-exponent, they suggested that once the approximate depth of an overpressured zone is known, the d-exponent curve can delineate its top boundary with high accuracy. The d-exponent method, however, requires a constant mud weight—a condition rarely met in practice. Increasing mud density within the pressure-transition zone exacerbates the chip-hold-down effect, reduces the ROP, and inflates the d-exponent, thereby distorting the diagnostic trend (Erivwo and Makis, 2021). To mitigate mud-weight effects, Rehm and McClendon (1971) introduced a corrected d-exponent, now widely known as the dc-index. In normally compacted strata, dc-index cluster along a baseline trend, whereas overpressured intervals deviate leftward; the magnitude of deviation is used to infer pressure variations. Nevertheless, because the dc-index is grounded in shale compaction laws and closely linked to framework strength, lithological changes alter that strength and, consequently, the dc-index. Moreover, variations in mud weight, annular pressure losses, and cuttings concentration during drilling continually modify bottom-hole differential pressure, further perturbing the dc-index. Additionally, the dc-index is derived from roller-cone bit equations and is therefore more applicable to such bits; modern PDC bits break rock via a markedly different mechanism, potentially biasing dc-based diagnostics. During the ensuing decades, researchers attempted to refine the dc approach; for example, Solano et al. (2007) in Colombia and Shajari (2013) in Iran incorporated local effective-stress-d-exponent correlations to stabilize the normal compaction trend and reduce subjectivity. Nevertheless, the intrinsic limitations remain unresolved, and the development of real-time drilling-data-based *P*p estimation has largely stagnated (Erivwo and Makis, 2021).

Because overpressured formations possess lower effective stress and thus require less energy for rock failure, several scholars introduced mechanical specific energy (MSE) as a diagnostic for *P*p. Rivas Cardona (2011) incorporated MSE into the Eaton equation, translating log data into drilling metrics for real-time *P*p estimation and proposing a novel methodology. Majidi et al. (2017) combined MSE with drilling efficiency (DE) to predict *P*p. Results from Gulf of Mexico deep-water wells aligned with sonic-log data and outperformed the classical dc-index. Rashidi and Asadi (2018) employed MSE and DE as inputs to an artificial neural network, obtaining *P*p estimates consistent with sonic logs and confirming that these parameters capture *P*p variations. Oloruntobi et al. (2018) proposed a hydro-rotary specific energy approach; field tests in Nigeria's Niger Delta marshes yielded magnitudes and trends consistent with measurements, demonstrating that coupling system energy with rock-breakage energy is effective for surface *P*p monitoring. Chen et al. (2024) combined MSE with the DE technique and applied it in the Ying-Qiong Basin, showing high correspondence between monitored and measured pressures. Despite the promising performance of combined MSE and DE diagnostics, several shortcomings persist in practical applications. First, previous studies did not rigorously select an MSE model; the resulting MSE values cannot approximate the rock's confined compressive strength (CCS) without additional DE corrections. Second, bottom-hole unconfined compressive strength (UCS) and internal friction angle (IFA) were fitted with simple power relationships to ROP, yielding imprecise estimates and potential bias. Finally, as exploration advances into deep water and deep formations, high-yield HTHP reservoirs are increasingly common. In such wells, mud properties vary significantly with temperature, and annular pressure losses and cuttings loading alter bottom-hole pressure (BHP), which can no longer be equated to the hydrostatic pressure.

To address these deficiencies, the present study develops a surface-based real-time HTHP *P*p estimation method that integrates MSE with rock-failure criteria. The flowchart of the proposed method is shown in Fig. 1. An MSE model that accurately represents CCS is first selected, obviating the need for supplementary DE corrections. Ridge regression is employed to invert bottom-hole rock parameters in real time, thereby reducing process errors. A transient thermo-pressure coupled solid–liquid two-phase flow model for HTHP wells is then constructed, enabling real-time BHP calculation from surface data and improving differential-pressure accuracy. The method is validated with field data from multiple HTHP wells in the South China Sea's Ying-Qiong Basin, demonstrating reliable and stable performance and offering the potential to enhance drilling safety while reducing costs.

2. New method for *P*p estimation in HTHP wells

2.1. Analysis of bottom-hole rock stress state under the Mohr-Coulomb failure criterion

The Mohr-Coulomb criterion is a classical theory for describing shear failure and is widely employed in rock mechanics and geotechnical engineering. Its fundamental form is

$$\tau = c + \sigma \tan\phi \tag{1}$$

where τ is the shear stress on the failure plane, c is the rock cohesion, σ is the normal stress, and ϕ is the IFA.

In principal-stress space, the Mohr circle represents the stress state defined by the maximum principal stress σ_1 and the minimum principal stress σ_3. Its center and radius are:

$$r_1 = \frac{\sigma_1 + \sigma_3}{2} \tag{2}$$

$$r_2 = \frac{\sigma_1 - \sigma_3}{2} \tag{3}$$

Rock reaches imminent failure when the Mohr circle is tangent to the failure envelope (1). Under uniaxial compression ($\sigma_3 = 0$), the unconfined compressive strength (UCS, σ_c) is obtained as:

$$\sigma_c = \frac{2c\cos\phi}{1 - \sin\phi} \tag{4}$$

For triaxial compression ($\sigma_3 \neq 0$), combining Eqs. (1) and (4) yields the maximum principal stress at failure:

$$\sigma_1 = \sigma_3 \frac{1 + \sin\phi}{1 - \sin\phi} + \sigma_c \tag{5}$$

Eq. (5) indicates that, under triaxial conditions, rock strength is controlled by both UCS and the IFA.

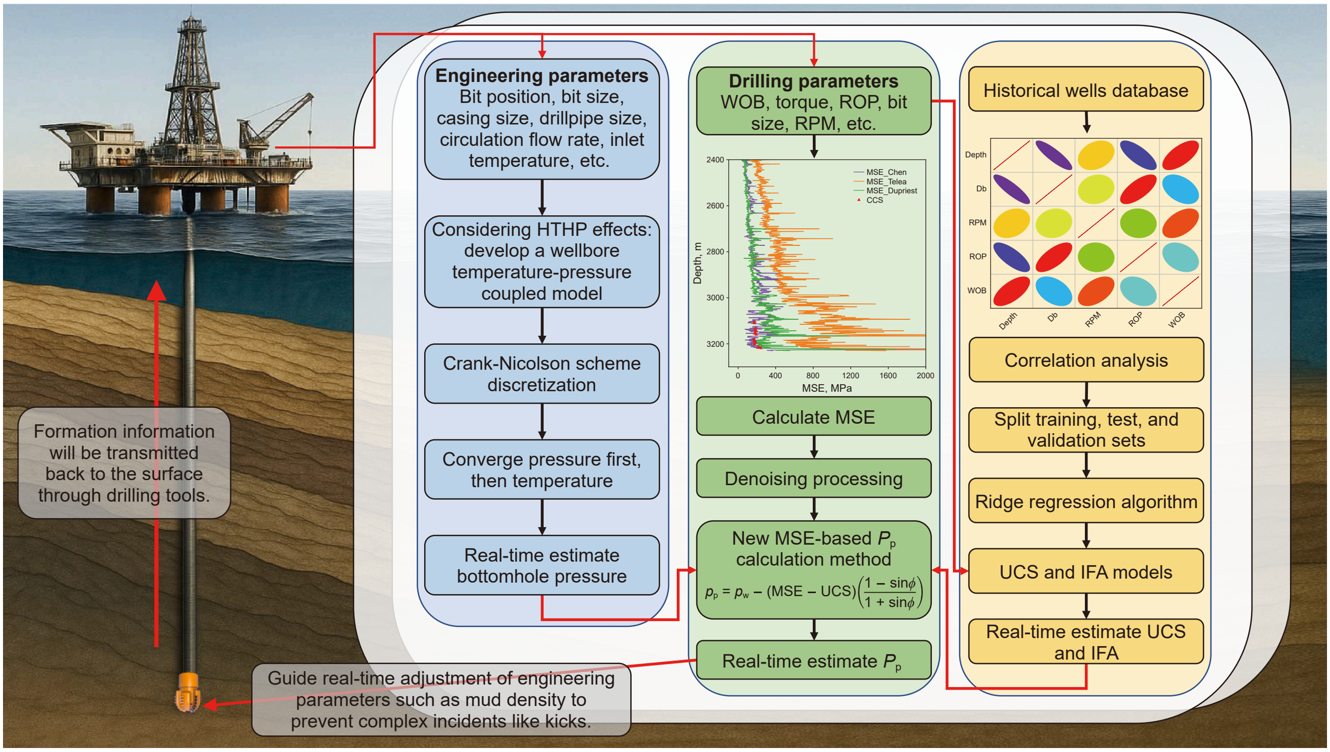

Fig. 1. Flowchart of the surface-based real-time HTHP *Pp* estimation method integrating MSE and rock-failure criteria.

At the bit, especially beneath the cutting elements, the confining stress σ_3 is generally treated as the differential pressure Δp between BHP and *Pp* (Liu et al., 2023). A decrease in Δp often enhances DE, a trend confirmed by underbalanced-drilling field observations: either encountering high *Pp* or keeping ECD below *Pp* can accelerate penetration (Caicedo et al., 2005). Accordingly, σ_3 may be replaced by Δp. Substituting CCS for σ_1 and UCS for σ_c yields the bottom-hole failure condition:

$$\mathrm{CCS} = \mathrm{UCS} + \Delta p \frac{1+\sin\phi}{1-\sin\phi} \tag{6}$$

Rearranging Eq. (6) expresses the *Pp* as:

$$p_\mathrm{p} = p_\mathrm{w} - (\mathrm{CCS} - \mathrm{UCS})\left(\frac{1-\sin\phi}{1+\sin\phi}\right) \tag{7}$$

where p_w is the BHP, and Δp is the difference between the BHP and the *Pp*.

2.2. Development of MSE model and characterization of bottom-hole rock strength

MSE, defined as the work done by the drilling system per unit rock volume excavated, is an indicator of mechanical efficiency. Teale (1965) showed that the minimum MSE correlates strongly with triaxial compressive strength, so that at high efficiency, MSE can be approximated as CCS. His original expression is:

$$\mathrm{MSE} = \frac{\mathrm{WOB}}{A_\mathrm{b}} + \frac{120\pi RT}{A_\mathrm{b}\mathrm{ROP}} \tag{8}$$

where WOB is weight on bits of surface measurement, lbf; A_b is bit area, in^2; R is bit rotating speed, rpm; T is torque, ft-lbs; ROP is rate of penetration, ft/h.

Considerable energy dissipates before reaching the bit, so field measured MSE is usually much higher than CCS. Accounting for frictional and mechanical losses, Dupriest and Koederitz (2005) assumed a bit peak efficiency of 30%–40% and fixed it at 0.35, giving:

$$\mathrm{MSE} = 0.35\left(\frac{\mathrm{WOB}}{A_\mathrm{b}} + \frac{120\pi RT}{A_\mathrm{b}\mathrm{ROP}}\right) \tag{9}$$

Chen et al. (2014) refined the equation using relationships among MSE, CCS, drilling parameters, and ROP. The surface calculated MSE aligns closely with log derived CCS and exhibits minimal variance, permitting MSE to be treated as CCS:

$$\mathrm{MSE} = E_\mathrm{m}\mathrm{WOB}_\mathrm{b}\left(\frac{1}{A_\mathrm{b}} + \frac{13.33\mu_\mathrm{b}R}{D_\mathrm{b}\mathrm{ROP}}\right) \tag{10}$$

$$\mathrm{WOB}_\mathrm{b} = \mathrm{WOB}{\cdot}\mathrm{e}^{-\mu\gamma_\mathrm{b}} \tag{11}$$

where, E_m is mechanical efficiency of new bit, dimensionless; μ_b is bit-specific coefficient of sliding friction, dimensionless; D_b is bit diameter, in; μ is coefficient of friction of drill string, dimensionless; γ_b is inclination of the bottom hole, rad.

Earlier studies frequently introduced DE to correct unstable MSE values, defined as:

$$\mathrm{DE} = \frac{\mathrm{CCS}}{\mathrm{MSE}} \tag{12}$$

However, this approach complicates operations and requires CCS, which is not readily available at surface. With Chen's model, MSE can be approximated as CCS. Thus, the pore-pressure equation becomes:

$$p_\mathrm{p} = p_\mathrm{w} - (\mathrm{MSE} - \mathrm{UCS})\left(\frac{1-\sin\phi}{1+\sin\phi}\right) \tag{13}$$

By performing a first-order approximation on the aforementioned formula, the uncertainty propagation law of each parameter is as follows:

$$\delta p_{\mathrm{p}} \approx \delta p_{\mathrm{w}} + r(\phi)(\delta\mathrm{UCS} - \delta\mathrm{MSE}) + (\mathrm{MSE} - \mathrm{UCS})\frac{\partial r}{\partial \phi}\delta\phi \tag{14}$$

where δPp, δP_{w}, δUCS, δMSE and $\delta\phi$ are the uncertainties of each parameter; $r(\phi)$ is a function determined by the IFA, $r(\phi) = \frac{1-\sin\phi}{1+\sin\phi}$, which reflects the influence of the IFA on uncertainty propagation; $\frac{\partial r}{\partial \phi}$ is the partial derivative of the function $r(\phi)$ with respect to ϕ, used to describe how the uncertainty $\delta\phi$ of the IFA affects the uncertainty of *P*p through the variation of $r(\phi)$. Three conclusions can be drawn from Eq. (14): The errors of UCS and MSE linearly affect the *P*p with opposite signs; The uncertainty of IFA only acts through $r(\phi)$ and is scaled by (MSE−UCS); The error in BHP is directly propagated to the final *P*p result.

2.3. Real-time inversion method for bottom-hole rock mechanical parameters based on ridge regression

Numerous ROP models—e.g., the Warren model and its modification, the Cunningham model, and the Renzo-Cesaroni model—contain a UCS term, allowing UCS back-calculation from mud-logging data (Hossain and Al-Majed, 2015). Yet their accuracy is strongly condition-dependent, and they may be unsuitable for the Ying-Qiong Basin. Furthermore, no empirical formula exists to estimate the IFA from surface data; traditionally IFA is derived from post-drilling sonic logs. Recently, Zhang et al. (2025) showed that mud logging data can predict UCS and IFA in real time, with mean absolute percentage errors below 0.71% and 2% in two wells. To ensure interpretability, this study employs ridge regression for online inversion of UCS and IFA during Ying-Qiong Basin drilling. Ridge regression adds an L2 penalty to the least-squares loss to alleviate multicollinearity and over-fitting; it is a variant of generalized linear models (Carneiro et al., 2022). The loss function is:

$$L(\xi) = \sum_{i=1}^{n}(y_i - X_i\xi)^2 + \lambda\sum_{j=1}^{p}\xi_j^2 \tag{15}$$

where λ is the regularization (penalty) parameter that sets the strength of penalization; ξ is the coefficient vector of the model; $\lambda\sum_{j=1}^{p}\xi_j^2$ is the L2 norm (sum of squared coefficients).

The penalty limits coefficient magnitude, preventing excessive complexity and over-fitting. Adjusting λ balances fit quality and model simplicity. The optimization goal is:

$$\min_{\xi}\left(\sum_{i=1}^{n}(y_i - X_i\xi)^2 + \lambda\sum_{j=1}^{p}\xi_j^2\right) \tag{16}$$

The solution is obtained via the normal equation:

$$\xi = \left(X^{\mathrm{T}}X + \lambda I\right)^{-1}X^{\mathrm{T}}y \tag{17}$$

This closed-form expression allows direct computation of ξ, obviating back-propagation.

2.4. Development of transient thermo-pressure coupled solid-liquid two-phase flow model for HTHP wells

Because BHP in HTHP wells cannot be simplified to a static mud column, we construct a coupled temperature-pressure solid–liquid two-phase-flow model to predict it accurately, subject to the following assumptions.

(1) The wellbore annulus contains a cuttings-mud solid–liquid two-phase flow.
(2) Flow is one-dimensional along depth.
(3) Solid and liquid phases share identical temperature and pressure at any given depth.

It is important to note that these assumptions are valid for conventional drilling operations. However, in the event of complex downhole conditions such as gas influx or severe circulation loss, the wellbore fluid transitions to a three-phase (gas–liquid–solid) flow regime. The current model is not designed to capture these physics and would therefore be inapplicable under such scenarios.

The flow laws of solid–liquid two-phase flow in the wellbore can be described by mass conservation, momentum conservation, and energy conservation. For the annular micro-control volume shown in Fig. 2, the continuity equations for the solid and liquid phases can be expressed as follows:

$$\frac{\partial}{\partial t}(\rho_s\alpha_s A) + \frac{\partial}{\partial z}(\rho_s\alpha_s v_s A) = q_s \tag{18}$$

$$\frac{\partial}{\partial t}(\rho_l\alpha_l A) + \frac{\partial}{\partial z}(\rho_l\alpha_l v_l A) = 0 \tag{19}$$

According to the law of momentum conservation, the momentum equations for the solid–liquid two-phase can be obtained as:

$$\begin{aligned}&\frac{\partial}{\partial t}(\rho_s\alpha_s v_s A + \rho_l\alpha_l v_l A) + \frac{\partial}{\partial z}\left(\rho_s\alpha_s v_s^2 A + \rho_l\alpha_l v_l^2 A\right) + (\rho_s\alpha_s \\ &\quad + \rho_l\alpha_l)g\sin(\theta)A + \frac{\partial}{\partial z}(pA) + A\frac{\partial p_f}{\partial z} \\ &\quad = q_s\end{aligned} \tag{20}$$

where, ρ_s and ρ_l are the solid and liquid densities, respectively, g/cm^3; α_s and α_l are the solid and liquid volume fractions, respectively, dimensionless; A is the annular cross-sectional area of the wellbore, m^2; v_s and v_l are the solid and liquid velocities, respectively, m/s; q_s is the rate of cuttings generation per unit thickness, kg/(s·m); g is the gravitational acceleration, taken as 9.81 m/s^2; θ is the angle between the wellbore direction and the horizontal, rad; p

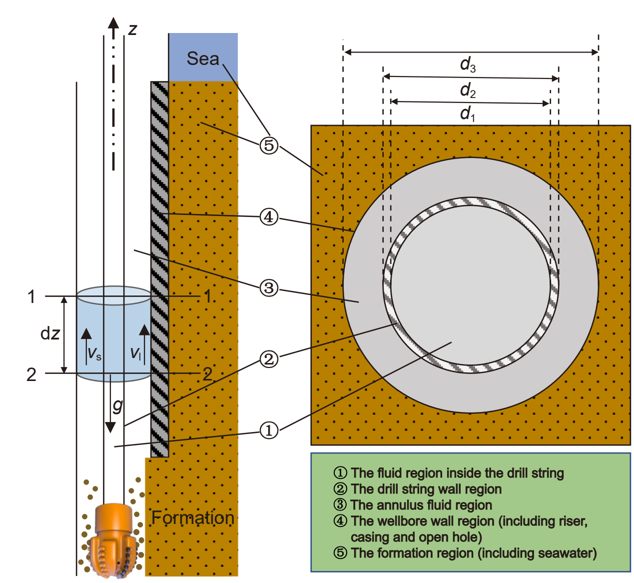

Fig. 2. Schematic of the wellbore heat transfer system and two-phase flow control volume.

is the pressure, Pa; p_f is the frictional pressure loss along the annulus, Pa.

The entire circulation process of the drilling fluid in the wellbore can be regarded as a heat exchanger with specific boundary conditions. The wellbore-formation heat transfer system can be radially divided into five regions, namely the fluid inside the drill string, the drill string wall, the annulus fluid, the wellbore wall (including riser, casing and open hole), and the formation. Therefore, an energy equation is respectively established for each region.

Drill string internal fluid:

$$\pi d_{p_i} U_{ap}\left[T_a - T_p\right] - \rho_p q_p C_p \frac{\partial T_p}{\partial z} + Q_{cp} = \frac{\pi d_{p_i}^2}{4}\rho_p C_p \frac{\partial T_p}{\partial t} \tag{21}$$

Annulus fluid in seawater section:

$$\begin{aligned}&\pi d_{ri} U_{sa}[T_s - T_a] - \pi d_{pi} U_{ap}\left[T_a - T_p\right] + \rho_a q_a C_a \frac{\partial T_a}{\partial z}\\&+ Q_p = \frac{\pi\left(d_{ri}^2 - d_{po}^2\right)}{4}\rho_a C_a \frac{\partial T_a}{\partial t}\end{aligned} \tag{22}$$

Annulus fluid in rock section:

$$\begin{aligned}&\pi d_w h_f\left[T_f - T_a\right] - \pi d_{pi} U_{ap}\left[T_a - T_p\right] + \rho_a q_a C_a \frac{\partial T_a}{\partial z}\\&+ Q_a = \frac{\pi\left(d_w^2 - d_{po}^2\right)}{4}\rho_a C_a \frac{\partial T_a}{\partial t}\end{aligned} \tag{23}$$

Seawater section formation:

$$\rho_{sa} C_s \frac{\partial T_s}{\partial t} = \lambda_s \frac{\partial^2 T_s}{\partial z^2} + \lambda_s \frac{\partial^2 T_s}{\partial r^2} + \frac{\lambda_s}{r}\frac{\partial T_s}{\partial r} \tag{24}$$

Rock section formation:

$$\rho_f C_f \frac{\partial T_f}{\partial t} = \lambda_f \frac{\partial^2 T_f}{\partial z^2} + \lambda_f \frac{\partial^2 T_f}{\partial r^2} + \frac{\lambda_f}{r}\frac{\partial T_f}{\partial r} \tag{25}$$

d_{pi}, d_{po}, d_{ri}, and d_w are the inner diameter of the drill pipe, outer diameter of the drill pipe, inner diameter of the riser, and inner diameter of the casing, respectively, m; U_{ap} and U_{sa} are the total heat transfer coefficients between the annular fluid and drill pipe inner fluid, and between seawater and annular fluid, respectively, W/(m^2·°C); T_p, T_a, T_s, and T_f are the temperatures of the drill pipe inner fluid, annular fluid, seawater, and formation rock, respectively, °C; ρ_p, ρ_a, and ρ_{sa} are the densities of the drill pipe inner fluid, annular fluid, and seawater, respectively, g/cm^3; q_p and q_a are the flow rates of the fluid inside the drill pipe and annular fluid, respectively, L/s; C_p, C_a, C_s, and C_f are the specific heats of the drill pipe inner fluid, annular fluid, seawater, and formation rock, respectively, J/(kg·°C); Q_p and Q_a are the viscous friction power of the fluid inside the drill pipe and annular fluid, respectively, W/m; h_f is the convective heat transfer coefficient, W/(m^2·°C); λ_s and λ_f are the thermal conductivities of seawater and formation rock, respectively, W/(m^2·°C); z is the axial coordinate, m; r is the longitudinal coordinate, m.

The mass conservation, momentum conservation, and energy conservation equations can describe the fundamental laws governing the fluid flow rate, wellbore pressure, and temperature changes with time and well depth for solid–liquid two-phase flow during drilling. However, multiple key parameters cannot be solved using only the above equations, thus it is necessary to introduce auxiliary equations:

$$\begin{cases}\alpha_s + \alpha_l = 1\\ v_s = a_0 v_{ef} - v_{sr}\\ v_{sr} = 0.223\dfrac{e^{5.03\chi}\mu_m}{\rho_m d_s}\sin(\theta)\left[\sqrt{1 + 0.399g\dfrac{(\rho_s - \rho_m)\rho_m d_s^3}{e^{5.03\chi}\mu_m^2}} - 1\right]\\ \dfrac{\partial p_f}{\partial z} = \dfrac{2f\rho_{ml}{v_{ml}}^2}{D}\\ \dfrac{1}{\sqrt{f}} = -4\log\left(0.269\dfrac{\varepsilon}{D} + \dfrac{1.255}{Re\sqrt{f}}\right)\end{cases} \tag{26}$$

where, a_0 is the solid phase distribution coefficient, dimensionless; v_{ef} is the effective return velocity, m/s; v_{sr} is the solid phase settling velocity, m/s; χ is the particle sphericity, dimensionless; μ_m is the plastic viscosity of the liquid phase around particles, mPa·s; ρ_m is the density of the liquid phase around particles, kg/m^3; d_s is the particle diameter, m; f is the Fanning friction factor, dimensionless; ρ_{ml} is the density of the liquid–solid mixture, kg/m^3; v_{ml} is the velocity of annulus fluid, m/s; D is the equivalent diameter, m; ε is the hydraulic roughness of circular tube, m; Re is the Reynolds number, dimensionless.

The pressure equation is discretised with a four-point explicit upwind scheme, whereas the temperature equation adopts an unconditionally stable fully implicit Crank-Nicolson scheme. For the boundary conditions, the wellhead back pressure remains constant, and the inlet temperature of the drilling fluid at the drill pipe is measurable. The temperatures of the drilling fluid inside the drill string, at the drill string wall, and in the annulus are equal at the bottom hole. The temperature at the outer boundary of the formation far from the wellbore is set to the original formation temperature. The distance from the outer boundary of the formation to the wellbore central axis is 3.05 m (Holmes and Swift, 1970). First-order spatial derivatives use upwind differencing. The pressure-equation time derivative employs a four-point central scheme, while the temperature equation uses a two-point backward difference for the first-order term and a three-point central difference for the second-order term. A nested iteration converges pressure first, then temperature, to obtain the full transient field. Because the model involves many parameters and empirical correlations and the present focus is on verifying MSE-based pore-pressure monitoring, readers are referred to (He, 2016; Wang et al., 2023; Yang et al., 2019, 2022) for details on initial/boundary conditions, discretisation, and solution procedures.

This transient model underpins the subsequent real-time determination of bottom-hole differential pressure from surface data and its coupling with MSE-UCS to compute *P*p.

3. Geological characteristics and parameter validation of the Ying-Qiong Basin

3.1. Geological setting and parameter characteristics

The validation of the proposed methodology was conducted mainly in Blocks M and N of the Ying-Qiong Basin, South China Sea. Its structural position and composite stratigraphic column are shown in Fig. 3. As the core area for hydrocarbon exploration in the

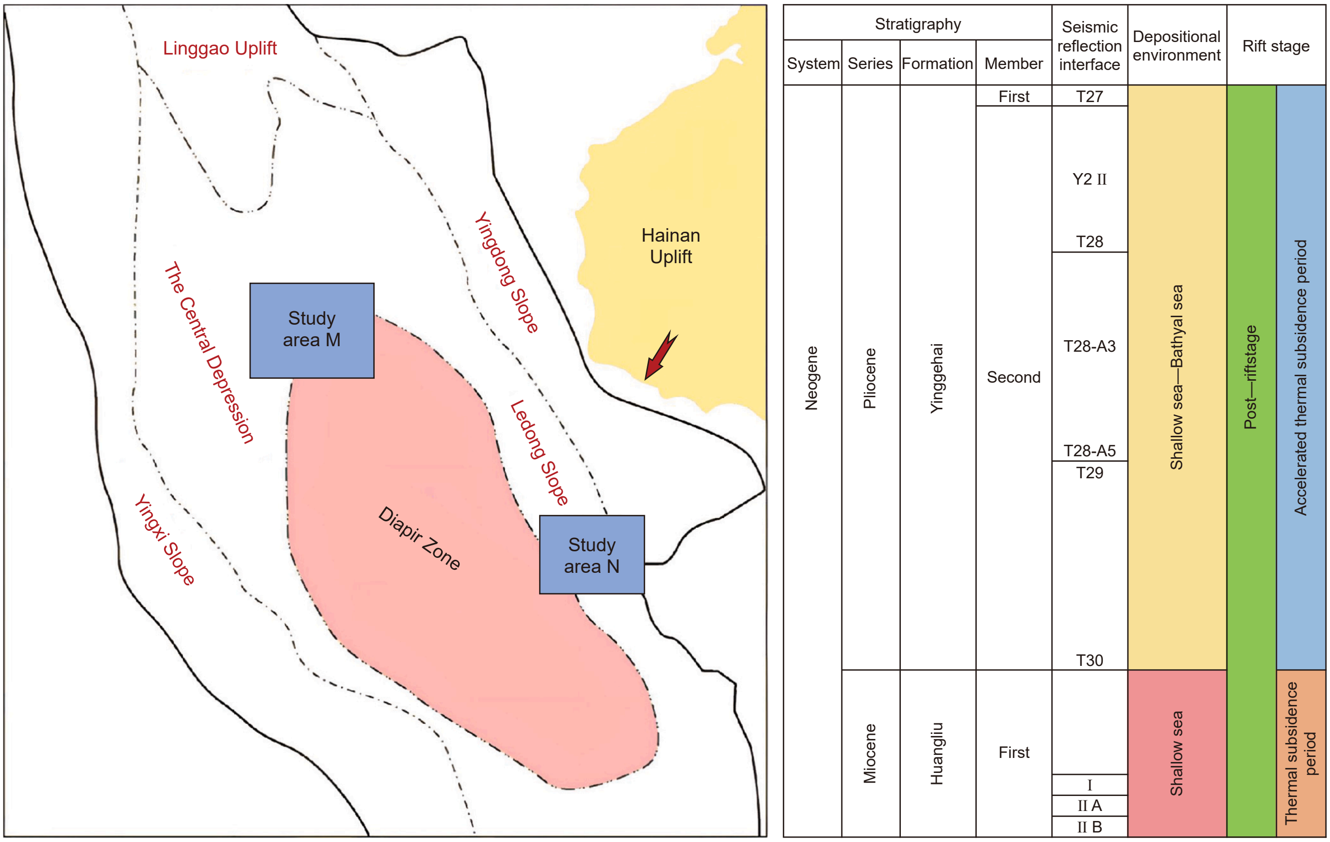

Fig. 3. Structural location and comprehensive stratigraphic column of the Ying-Qiong Basin (Caicedo et al., 2005).

western South China Sea, Ying-Qiong Basin is characterized by pronounced HTHP conditions: temperatures in some target formations reach 240 °C, pressure coefficients are as high as 2.30, and the pressure window is extremely narrow, posing serious challenges to safe drilling operations (Long et al., 2024; Zhang et al., 2013). Geological analyses indicate a complex overpressure genesis controlled by multi-phase hydrothermal circulation, diapiric tectonism, high-temperature hydrocarbon generation, and undercompaction resulting from rapid sedimentation. Three drilled-well datasets from Block N and eight drilled-well datasets from Block M were selected for analysis. The sonic-density crossplot (Fig. 4) indicates that the velocity-density trend in Block N suggests a composite mechanism of undercompaction and overpressure from hydrocarbon generation, whereas the trend in Block M exhibits the classic signature of undercompacted overpressure. The sonic-density data for Block N clearly deviates from the undercompaction trend line and shifts towards the fluid expansion trend line, which effectively supports a composite mechanism involving undercompaction and hydrocarbon generation overpressure (Guo et al., 2022). For Block M, this finding is consistent with its regional depositional history—three major rapid-sedimentation events, with central-basin rates generally exceeding 400 m/Ma and locally reaching 800–1000 m/Ma. This evidence confirms that overpressure in Block M is chiefly the result of undercompaction loading caused by rapid burial.

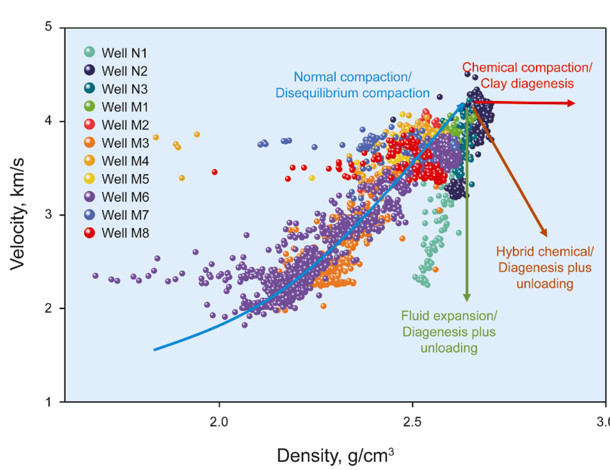

Fig. 4. Crossplot of log-derived sonic velocity and rock density in Blocks M and N.

Fig. 5 presents the log-and-drilling-parameter response of Well A within the study block, illustrating the depth profiles of natural gamma ray (GR), interval transit time (DT), rock density (RockDen), bit diameter (D_b), revolutions per minute (RPM), ROP, WOB, dc-index (DC), and *P*p (obtained by the Eaton method) from 2400 to 3250 m. The figure displays the typical undercompaction-induced overpressure response in the Huangliu Formation of Well A, while providing direct evidence of the coupling between drilling parameters and BHP. The GR curve is high between 2400 and 3000 m, indicating a clay-rich shale succession; at 3000 m GR decreases to 80–110 gAPI and remains low, revealing an overpressure window where reduced clay content coincides with local pressure release. Consistently, the DT curve increases sharply with fluctuations at 3000 m. RockDen generally increases with depth, but drops locally where DT spikes, producing a DT-up/RockDen-down combination—a classic signal of increased pore-fluid pressure and insufficient framework compaction. Step changes in RPM

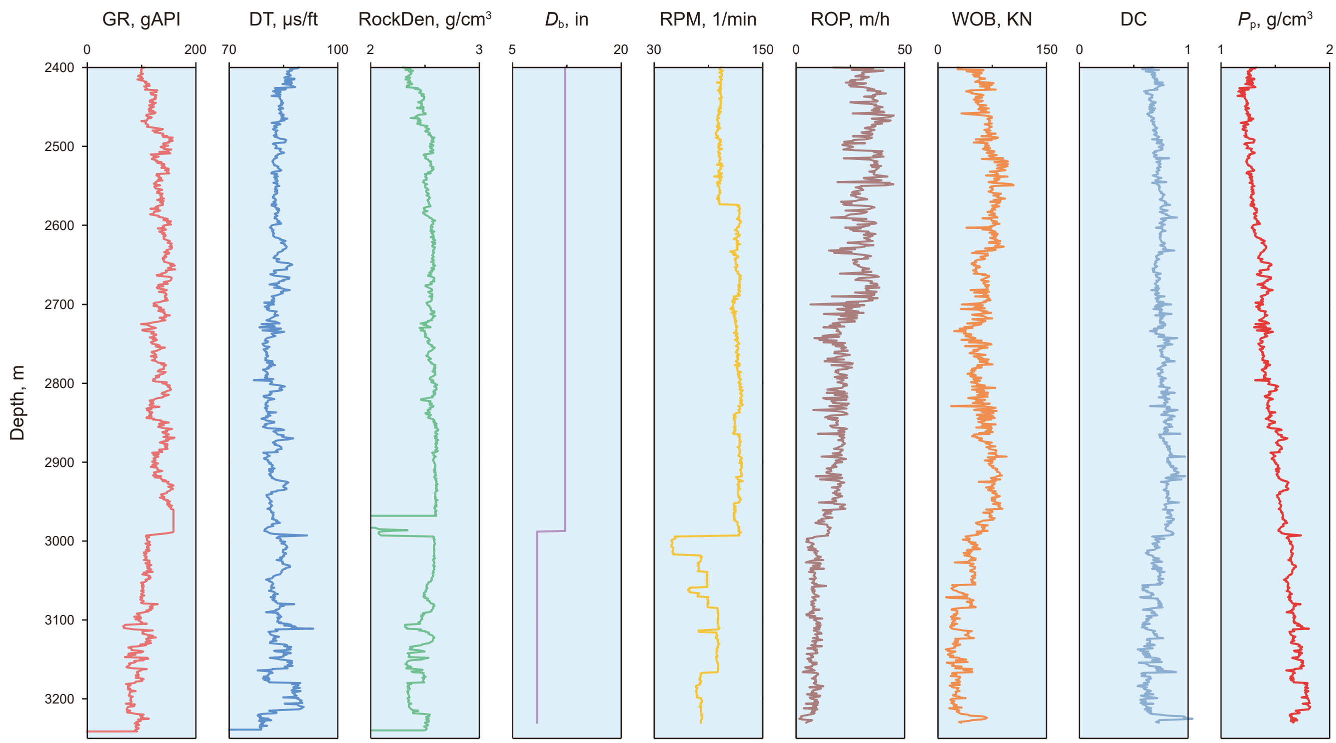

Fig. 5. Depth profiles of log and drilling parameters in Well A.

at 2575 m and deeper reflect adjustments in bit strategy for harder formations. ROP decreases overall with depth, yet at the 3000 m pressure step WOB drops slightly while ROP rebounds, indicating a reduced bottom-hole differential pressure and a corresponding decrease in MSE. The dc-index remains at 0.7–0.9 in normally compacted strata, but shifts leftwards to about 0.65 at 3000 m, further verifying a drilling-rate response to overpressure. The kink in *P*p calculated by the Eaton method also occurs at 3000 m, coinciding with the log-and-drilling-parameter inflection, thereby pinpointing the true pressure step. The synchrony of these multiple anomalies not only constrains the overpressure window in the Huangliu Formation of Well A but also furnishes direct field evidence for the subsequent drilling-parameter-based real-time pore-pressure monitoring method.

3.2. Model validation for real-time inversion of bottom-hole rock mechanical parameters

Conventional approaches that derive UCS from ROP equations depend heavily on empirical coefficients, and existing formulas for calculating the IFA from mud-logging data remain inadequate. Considering the high-dimensional correlation and overfitting risk of drilling data, ridge regression is selected as the regularization method. To overcome these limitations, ridge-regression algorithms were applied to historical drilling data from the Ying-Qiong Basin to develop machine-learning models capable of predicting UCS and the internal-friction angle in real time during drilling. The dataset was randomly divided into training, validation, and test sets in a 6:2:2 ratio to enable rigorous model assessment (Radwan et al., 2022). The ridge-regression models predicting UCS and the internal-friction angle used drilling parameters—WOB, RPM, D_b, and ROP—as input features. Figs. 6 and 7 illustrate the performance of the UCS and IFA models. High coefficients of determination were observed in both the validation set ($R^2 = 0.971$ for UCS and 0.969 for IFA) and the test set ($R^2 = 0.966$ for UCS and 0.964 for IFA), attesting to their excellent predictive capability. These findings confirm that ridge regression can reliably estimate downhole rock-strength properties from surface drilling parameters with outstanding generalization and robustness.

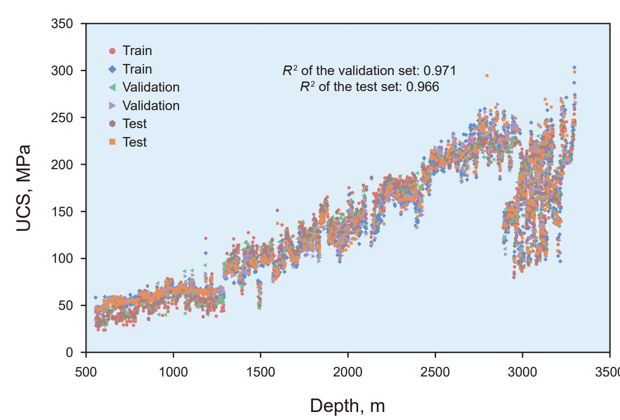

Fig. 6. UCS prediction model based on ridge regression across training, validation, and test datasets.

To evaluate the effectiveness of the machine-learning approach, the ridge-regression model was compared with two existing physical models: the Warren model and the Renzo Cesaroni model. Fig. 8 visualizes the comparison between predicted UCS from the three models and the true UCS derived from well logs. The comparison shows that, although both physical models capture the overall trend of UCS with depth, they exhibit significant numerical deviations from the true values. In contrast, the ridge-regression model not only fits the trend more closely but also matches the true UCS values with higher numerical accuracy and convergence. At shallower depths, the physical models are relatively consistent with each other yet still underestimate UCS

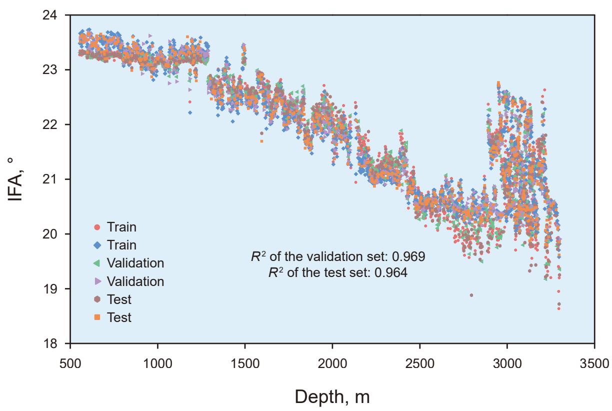

Fig. 7. IFA prediction model based on ridge regression across training, validation, and test datasets.

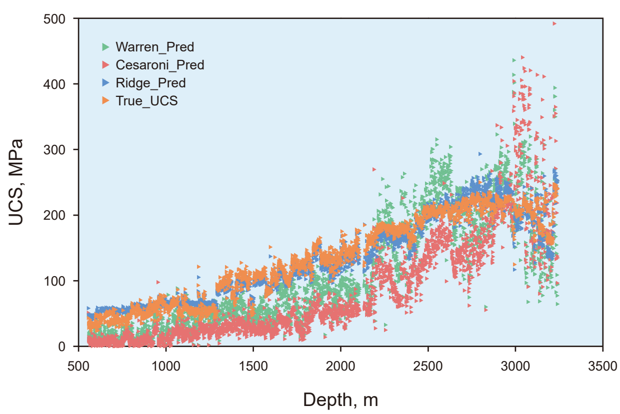

Fig. 8. Comparison of predicted vs. actual UCS in Well A from three models.

relative to log-derived measurements; at greater depths where lithological variation is more pronounced, their scatter increases and they only qualitatively track UCS variations. These observations highlight a fundamental limitation of traditional empirical models: they can only qualitatively indicate changes in downhole rock strength, whereas the machine-learning approach delivers far more accurate quantitative predictions.

Comprehensive error metrics listed in Table 1 further corroborate the superiority of the ridge-regression model. Compared with the Warren model (RMSE (root-mean-square error) = 50.06 MPa, MAE (mean absolute error) = 41.78 MPa) and the Renzo Cesaroni model (RMSE = 76.19 MPa, MAE = 62.37 MPa), the machine-learning model yields substantially lower RMSE (11.36 MPa) and MAE (10.00 MPa). Notably, the ridge-regression model attains an R^2 of 0.97, far surpassing the Warren model ($R^2 = 0.39$) and the Renzo Cesaroni model ($R^2 = -0.42$, indicating poor fit). Mean error (ME) and mean squared error (MSEr) indicators likewise confirm the significant improvements afforded by the machine-learning approach. These results demonstrate that the proposed ridge-regression model is highly reliable for real-time estimation of downhole rock-strength parameters in Ying-Qiong Basin drilling operations and can effectively underpin the pore-pressure calculations presented in this study.

Table 1
Comparison of error metrics for UCS prediction in Well A from three models.

Model	RMSE	MAE	R^2	ME	MSEr
Ridge	11.36	10.00	0.97	43.23	129.05
Warren	50.06	41.78	0.39	268.82	2506.04
Cesaroni	76.19	62.37	−0.42	934.17	5804.99

3.3. *Model validation for BHP in HTHP wells*

In HTHP environments, the physical properties of drilling fluids, such as density and viscosity, are significantly affected by temperature and pressure. Concurrently, drill cuttings generated during the process alter the mixture density and rheology of the fluid within the annulus. Consequently, the static hydrostatic pressure calculated solely from surface fluid density fails to accurately reflect the true BHP, introducing significant computational errors. To precisely monitor *P*p in HTHP wells, it is imperative to first establish a dynamic model that accurately describes the BHP. This section aims to validate the accuracy of the transient thermo-pressure coupled model proposed herein, using measured field data, and to thoroughly analyze the discrepancies between the model's predictions and actual measurements.

Well A from the study area was selected as a case for validation; its key simulation parameters are listed in Table 2. The well has a total depth of 3240 m, a water depth of 67 m, and a geothermal gradient of 4.196 °C/100 m, with a sea-surface temperature of 30 °C. The selected interval covers a critical pressure transition zone. The wellbore thermo-pressure model was used to simulate drilling from 3000 to 3230 m in 10-m increments. Over this interval, drilling-fluid density ranges from 1.72 to 1.78 g/cm^3, flow rate from 25.12 to 28.52 L/s, mechanical penetration rate from 4.7 to 10.51 m·h^{-1}, and fluid inlet temperature from 54.5 to 57.8 °C. The final bottom-hole assembly comprised 8-3/8″PDC+F/V+6-3/4″EcoScope+6-3/4″TeleSccope+8-1/8″STAB+X/O+6-1/2″DC*13+X/O+JAR+F/J+5″HWDP*14+5″DP.

Figs. 9 and 10 demonstrate the model's predictive performance for temperature and pressure, respectively. Fig. 9 compares the model-predicted outlet and annular bottom-hole temperatures against measured field data. The results reveal a MAE of just 0.93 °C for the outlet temperature and 2.23 °C for the annular

Table 2
Partial key parameters of the transient thermo-pressure coupled model for Well A.

Parameters	Numerical value	Parameters	Numerical value
Well depth, m	3000–3230	Surface temperature, °C	30
Water depth, m	67	Geothermal gradient, °C/100 m	4.196
Target horizon	Huangliu	Drilling fluid injection temperature, °C	54.5–57.8
Depth of the first spud, m	177	Specific heat capacity of drilling fluid, J/(kg·°C)	3900
Depth of the second spud, m	555	Specific heat capacity of drill pipe and casing, J/(kg·°C)	400
Depth of the third spud, m	2150	Specific heat capacity of formation rock, J/(kg·°C)	837
Depth of the fourth spud, m	2988	Thermal conductivity of drilling fluid, W/(m·°C)	1.73
Size of riser pipe, in	30	Thermal conductivity of drill pipe and casing, W/(m·°C)	43.75
Inner diameter of fourth-open casing, in	9-5/8	Thermal conductivity of formation rock, W/(m·°C)	2.25
Bit size, in	8-3/8	Flow rate, L/s	25.12–28.52
Total flow area of bit, in^2	1.09	Density of drilling fluid, g/cm^3	1.72–1.78

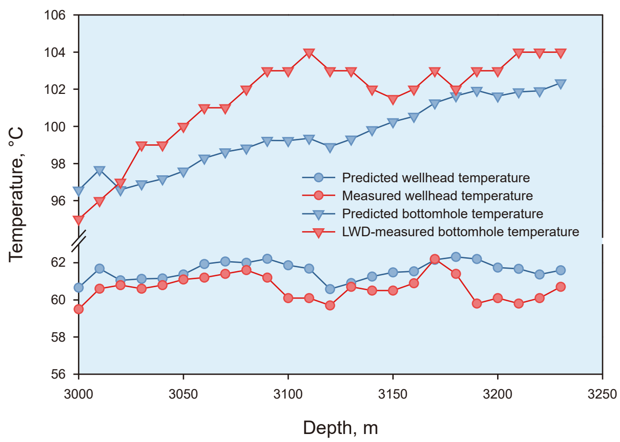

Fig. 9. Predicted vs. measured temperatures using the coupled model.

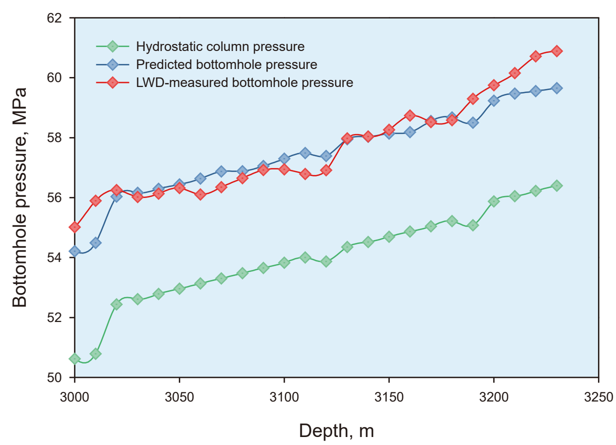

Fig. 10. Predicted vs. measured annular BHP using the coupled model.

bottom-hole temperature. This demonstrates that the model's heat transfer module accurately captures the dynamic temperature profile within the wellbore, establishing a solid foundation for precise pressure field calculations. In terms of bottom-hole pressure prediction, the conventional static hydrostatic method yields a substantial MAE of 3.64 MPa, highlighting its severe limitations in HTHP conditions. In contrast, the annular BHP predicted by the thermo-pressure coupled model developed in this study shows excellent agreement with the measured values, with an MAE of only 0.46 MPa. This result not only numerically proves the model's superior accuracy but also confirms mechanistically that comprehensively considering the effects of temperature on density, annular pressure loss, and cuttings transport is a prerequisite for achieving accurate pressure monitoring in HTHP wells.

Although the model performs well overall, prediction discrepancies at specific depths serve to reveal complex downhole dynamic events. A notable anomaly occurs near a depth of 3110 m. At this point, not only did the predicted annular BHP exhibit a local peak deviation of 0.69 MPa, but the predicted annular bottom-hole and outlet temperatures also reached their maximum errors simultaneously, at 4.64 and 1.59 °C, respectively. This synchronous anomaly in pressure and temperature predictions at the same depth suggests a complex situation occurred in the wellbore that was beyond the model's base assumptions. Upon reviewing the well's mud logging report, we discovered that total gas readings rose sharply from 5059 ppm at 3089 m to a peak of 82,715 ppm at 3107 m. This provides strong evidence of a gas influx event into the wellbore during this period. Based on this fact, the observed discrepancies can be reasonably explained: ① After gas invasion, the gas—with a density much lower than that of the drilling fluid—displaces part of the liquid column in the annulus, leading to a decrease in the density of the annular mixed fluid and consequently a drop in the measured bottomhole pressure. However, the model is established based on solid–liquid two-phase flow and does not account for the presence of the gas phase; its predicted pressure remains based on the drilling fluid density unaffected by the invasion. As a result, the predicted value is higher than the measured value, giving rise to the observed pressure deviation. ② The impact of gas invasion on the temperature field manifests in two aspects. First, the gas expands during its upward migration. According to the Joule-Thomson effect, this process affects the wellbore temperature, resulting in an increase in the measured annular bottomhole temperature. Second, the presence of gas accelerates the return velocity of the annular fluid, which shortens the heat exchange time between the drilling fluid and the high-temperature formation. Thus, the temperature of the drilling fluid returned to the wellhead (outlet temperature) is lower than the value predicted by the model. This is fully consistent with the phenomenon observed in Fig. 9, where the predicted annular bottomhole temperature is lower while the predicted outlet temperature is higher.

In summary, through comparative verification with field measured data, the transient thermal-pressure coupled model established in this study can accurately describe the temperature and pressure distributions in HTHP wellbores, thereby providing reliable bottomhole pressure input and dynamic condition constraints for the subsequent achievement of higher-precision *Pp* monitoring.

4. Results and discussion

4.1. Comparison of calculation stability of different MSE models

Fig. 11 compares the surface-calculated MSE for Well A using the Teale, Dupriest, and Chen models. CCS, used as a reference, was back-calculated from in-situ MDT pore-pressure measurements according to Eq. (6). In the shallow section of Well A (<3000 m), the MSE traces derived from the Chen and Dupriest models exhibit comparable stability. Beyond 3000 m, in the overpressured reservoir interval, the Dupriest curve becomes highly erratic owing to its fixed mechanical-efficiency assumption (0.35), whereas the Chen curve remains smooth because bottom-hole weight-on-bit and torque are dynamically corrected.

Mechanistically, the models differ significantly. The Teale model is based on an ideal rock-breaking assumption, ignoring borehole friction, inclination effects, efficiency decay, and bottom-hole differential pressure, which leads to a systematic overestimation of MSE at depth. The Dupriest model introduces a constant efficiency factor; however, this approach relies on a fixed,

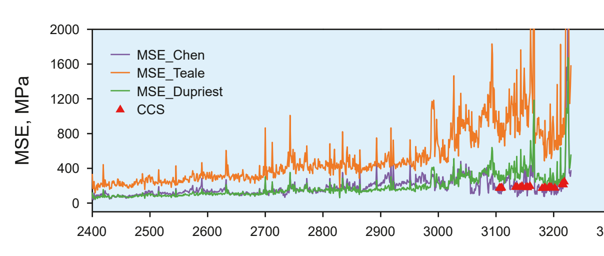

Fig. 11. Comparison of calculation results of different MSE models with CCS in Well A.

empirical mechanical efficiency coefficient (e.g., 0.35), a practice that is controversial because mechanical efficiency can vary significantly. Furthermore, the model still neglects inclination/friction distortion, annular pressure losses, and bit-dynamics corrections, making its curve sensitive to short-period disturbances and highly volatile.

In contrast, the Chen model overcomes these empirical simplifications by introducing a mechanistic model. Its core improvement is the calculation of the actual bottom-hole weight-on-bit by correcting for borehole friction and hole inclination. This mechanistic correction is embodied by the dynamic adjustment of bottom-hole WOB and torque. This correction enables the MSE calculation to be based on the "energy actually transferred to the rock surface" rather than on surface-measured energy distorted by drill-string friction. This represents a critical step forward from an empirical approximation to a model that more closely aligns with physical reality, marking a significant conceptual advancement.

Furthermore, because the Chen model more accurately calculates the energy at the bit, the resulting MSE value can be "directly used as an approximation of the CCS" without requiring additional DE correction. This improvement not only simplifies the procedure but, more importantly, establishes a more direct and robust physical link between a real-time engineering parameter and a fundamental rock mechanics property. From a practical application standpoint, because engineers no longer need to estimate a DE coefficient, the real-time monitoring process is simplified. This reduces subjectivity and potential human error, making the method more robust, reproducible, and easier to implement across different drilling platforms and operational teams. It is due to these improvements that the Chen model yields the best agreement with CCS and the lowest overall variance.

Given that mud-logging measurements may suffer from random errors and transient operational changes can introduce spurious spikes, outliers in the computed MSE series were removed and a moving-window average was applied to further de-noise the data.

4.2. Analysis of the impact of bottom-hole pressure solution methods on pressure monitoring results in HTHP wells

In the final hole section of Wells A and B, annular ECD and annular temperature were acquired in real time by logging-while-drilling (LWD) tools. To quantify how BHP estimation affects *P*p monitoring accuracy, three *P*w scenarios were substituted into Eq. (13): (i) hydrostatic-equivalent mud density (hydrostatic), (ii) LWD-measured bottom-hole density (LWD-measured), and (iii) the density predicted by the transient HTHP two-phase-flow model (HTHP-model). Comparative results are presented in Figs. 12 and 13.

Quantitatively, the hydrostatic-based *P*p_MSE_Den (*P*p estimated based on the MSE method and mud density) approach deviates markedly from the *P*p_MSE_LWD (*P*p estimated based on the MSE method and LWD measurements): the maximum density discrepancy reaches 0.184 g/cm^3 and the MAE is 0.099 g/cm^3 across the two wells. By contrast, the Pp_MSE_HTHP (*P*p estimated based on the MSE method and the thermo-pressure coupling model) variant, which incorporates temperature–pressure coupling, reduces the maximum discrepancy to 0.098 g/cm^3 and the MAE to only 0.014 g/cm^3—an improvement of more than six-fold over the hydrostatic assumption.

These findings corroborate the pressure-difference ratios shown in Fig. 10, underscoring the pronounced impact of temperature-induced density variations and annular friction losses on BHP in HTHP settings. Neglecting such multiphysics coupling yields systematic over- or under-estimation of *P*p,

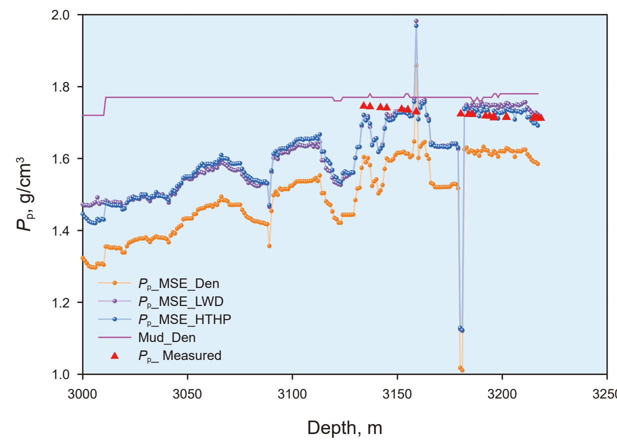

Fig. 12. Comparison of *P*p predictions using modeled, hydrostatic, and measured BHP in Well A.

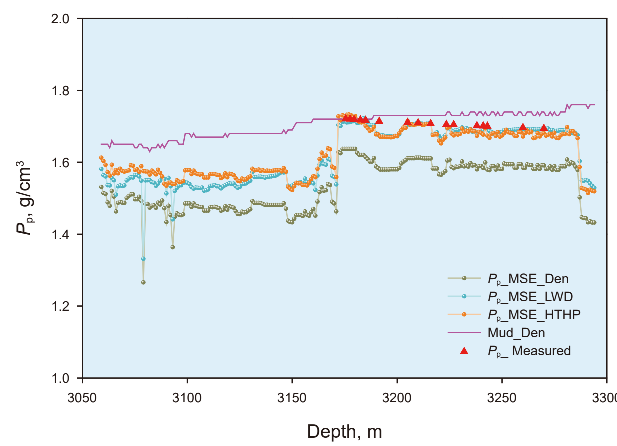

Fig. 13. Comparison of *P*p predictions using modeled, hydrostatic, and measured BHP in Well B.

whereas the transient model—driven by real-time wellbore parameters—effectively corrects the inherent bias of the hydrostatic assumption and furnishes the prerequisite for high-accuracy pressure surveillance.

Notably, the initial implementation of the model relied on dense matrix operations and the Gauss-Seidel iterative method to solve the linear system; however, modern numerical optimization techniques can substantially improve computational efficiency. In this study, several key optimizations were introduced: (i) replacing dense matrix operations with sparse matrix structures to reduce memory overhead and computational complexity, (ii) employing the backslash operator as a sparse linear solver to achieve superior performance, (iii) implementing an adaptive relaxation factor to enhance convergence stability and reduce the number of required iterations, and (iv) extensively vectorizing geometric parameter calculations and property evaluations to minimize computational loops. Under the same hardware configuration (AMD Ryzen 7 8845H), these optimizations reduced the single-point computation time from 874 to 68 s, a level of efficiency that can be regarded as sufficient to meet real-time requirements under practical drilling conditions.

4.3. Comparative analysis of different Pp evaluation models

To further demonstrate the reliability and advantages of the proposed approach for monitoring *P*p, formation pressures in five

Ying-Qiong wells were computed with the new MSE-based method and compared with results from the sonic-transit-time Eaton method (or Bowers method), the dc-index method, and MDT measurements (Fig. 14). These wells cover different overpressure origins: the overpressure in Wells A, B, C, and D is attributed to a loading genetic mechanism, while Well E exhibits a combined mechanism of loading and unloading. At ~3000 m in Well A, ~3175 m in Well B, and ~3075 m in Well D, all three methods—*P*p_MSE_HTHP, dc-index, and Eaton—display a sharp rise in the pressure coefficient, consistent with the "pressure-step" phenomenon reported for the Huangliu Formation (Fan et al., 2021). This concurrence indicates that both *P*p_MSE_HTHP and the dc-index respond sensitively to abrupt pressure changes.

In terms of accuracy, both *P*p_MSE_HTHP and the dc-index perform well in Well A, matching MDT data at depth. In Wells B and D, however, the dc-index diverges appreciably from the Eaton method over large depth intervals. Specifically, in Well B, the dc-index underestimates *P*p by ~0.2 g/cm^3 between 3050 and 3175 m, but overshoots after the pressure-step at 3175 m. In Well D, *P*p_MSE_HTHP and the dc-index share the same trend, yet the dc-index exceeds MDT *P*p between 3075 and 3125 m, whereas *P*p_MSE_HTHP aligns with MDT. In Well C, at 3050 m, *P*p_MSE_HTHP slightly underestimates *P*p relative to MDT, while the dc-index remains consistent with the measurement. In Well E, the *P*p_MSE_HTHP calculation is slightly high before 4050 m while the dc-index is low; after this depth, both methods align well with the MDT data. Notably in Well E, sudden decreases in the measured sonic transit time between 4096 and 4123 m and again between 4142 and 4165 m—possibly due to instrumental error—cause anomalies in calculations from the Bowers method. Nevertheless, both the *P*p_MSE_HTHP and dc-index methods remain consistent with MDT measurements through these intervals, demonstrating that both are relatively reliable.

To quantify the performance gap between the two pore-pressure monitoring techniques, the relative errors of the dc-index and MSE approaches were compared (Fig. 15). The error envelopes reveal that the relative error of the MSE method remains largely within 5% over the entire wellbore, whereas that of the dc-index widens considerably, extending to ±10%. As illustrated in Fig. 16, the MAE of the MSE approach are 6.29%, 1.70%, 4.03%, 3.44% and 1.13% for Wells A–E, yielding an overall MAE of 4.12% when calculated across all data points from the five wells, which indicates notable unbiasedness and convergence. By comparison, the dc-index produces MAE of 4.61%, 7.53%, 4.7%, 7.24% and 2.63%, corresponding to an overall MAE of 5.78%. Taken together, the error envelopes and statistical metrics show that, although both techniques track formation-pressure trends, the MSE method—thanks to the physical coupling between MSE and rock strength, supplemented by dynamic BHP correction—delivers superior accuracy and stability across diverse well conditions.

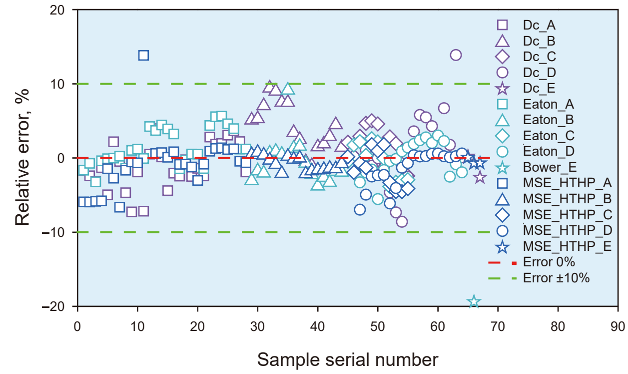

Fig. 15. Error analysis of different *P*p estimation models against MDT measurements.

4.4. Discussion of limitations and future prospects

The transient thermo-pressure model employed in this study assumes a Newtonian mud with entrained cuttings filling the annulus—an acceptable simplification for conventional rotary drilling. Under gas-influx or severe-loss scenarios, however, the

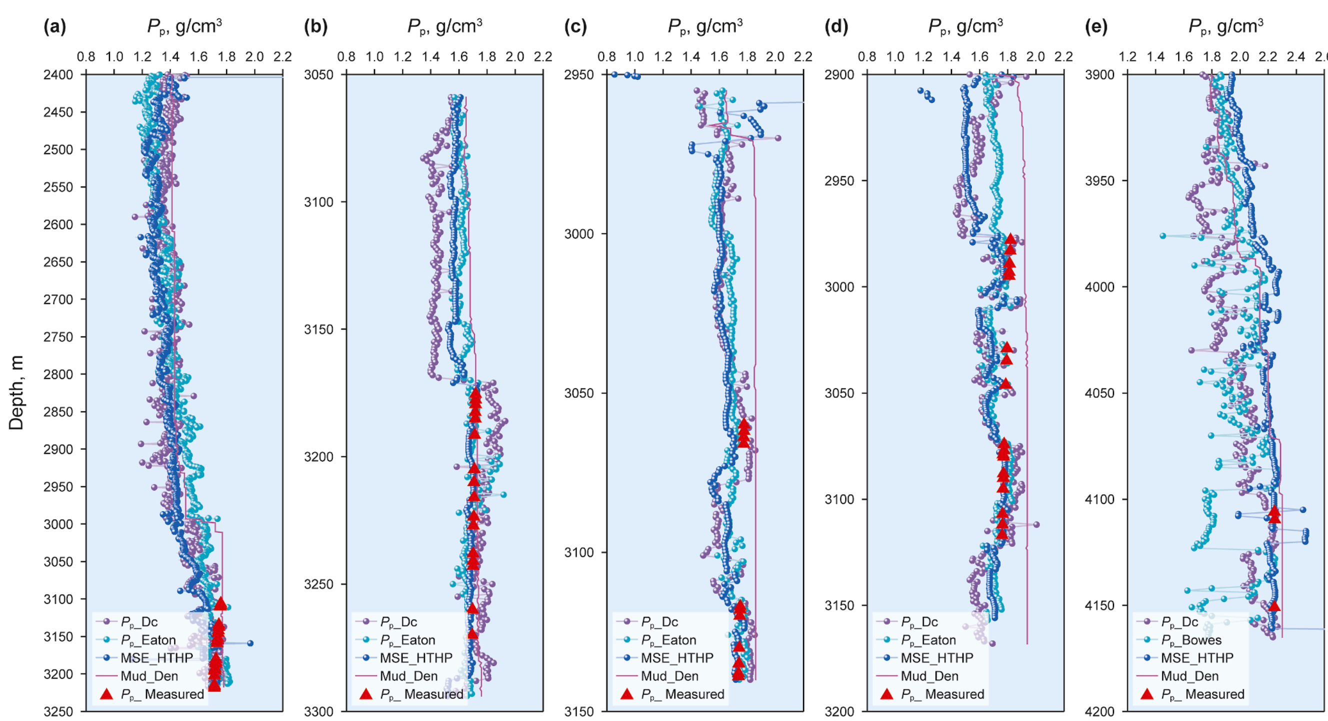

Fig. 14. Comparative analysis of different *P*p estimation models.

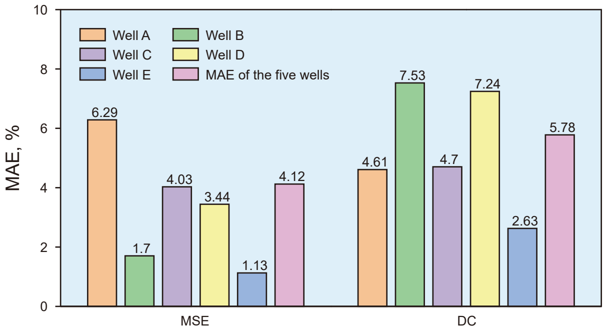

Fig. 16. Comparison of MAE of MSE method and dc-index method relative to MDT measured values.

pressure profile, temperature gradient, and frictional losses change markedly. Because the present model cannot capture BHP under such conditions, the calculated ECD may deviate significantly and propagate through Eq. (13) into the pore-pressure estimate. This limitation explains the isolated mismatch observed at 3090–3120 m in Well A. Notably, if an advanced multiphase simulator coupled with surface data could provide accurate BHP during gas influx or severe loss conditions, the principle of this framework could still be used to estimate *P*p. This would significantly extend its application scope. For example, it would enable real-time *P*p estimation in challenging scenarios, such as drilling through fractured formations with liberated gas influx using managed pressure drilling, thus providing direct guidance for optimizing critical managed pressure drilling parameters.

However, such an extension shifts the challenge to the accuracy of the multiphase model itself and, more critically, the acquisition of its boundary conditions. Specifically, the “unobservability” of critical downhole parameters from the surface—such as the real-time gas influx rate and volume—severely constrains the acquisition of these necessary boundary conditions. Therefore, a paradigm shift from surface-based inference to downhole-based estimation is the key to overcoming this challenge. Future work should focus on embedding the entire computational workflow developed in this study onto a downhole smart tool. Such a system would acquire high-frequency local data—such as while-drilling acoustic velocity, dual-point pressure/temperature, and bit-axis vibration—and execute the integrated MSE and rock mechanics calculations in-situ using an onboard processor. Crucially, instead of transmitting large volumes of raw data, only the final computed *P*p value would be sent to the surface via MWD mud-pulse telemetry. This approach would not only maximize accuracy by using direct, real-time measurements but also provide the timeliest possible warning, fundamentally solving the problem of information delay and uncertainty inherent in surface models.

5. Conclusions

We developed a pore-pressure prediction workflow for HTHP wells that relies exclusively on real-time surface data. The approach couples a refined MSE model with the Mohr-Coulomb failure criterion and replaces the hydrostatic assumption with a solid-liquid transient thermo-pressure model to compute BHP. The resulting closed-form solution is mechanistically transparent, computationally efficient, and circumvents the large uncertainties of seismic/log methods, dc-index misdiagnoses, and the high cost of downhole acoustics.

Case studies of Wells A and B demonstrate that the Chen MSE model is more stable than the traditional Teale and Dupriest models and can be approximated as CCS, eliminating empirical efficiency factors. Incorporating temperature-pressure coupling lowers the average error of the *P*p-equivalent density by 0.085 g/cm^3 relative to the hydrostatic estimate, confirming that temperature, annular friction, and hydraulic losses are non-negligible in HTHP wells.

In five Ying-Qiong wells, both the MSE-HTHP method and the dc-index accurately captured the characteristic “pressure-step” in the Huangliu Formation; however, the MSE-HTHP relative error remains within ±5%, compared with ±10% for the dc-index, demonstrating the superior robustness of the proposed framework under varied well conditions and pressure regimes. Furthermore, the overall MAE of the MSE-HTHP method across the five wells is 4.12%, compared to 5.78% for the dc method, highlighting the advantage of the MSE approach for estimating *P*p from the surface.

Because the workflow relies solely on surface measurements, it offers an economical and efficient means of monitoring *P*p, enabling real-time mud-weight optimization and early kick detection—key requirements for risk-based drilling. Above all, the study shows that deep integration of rock-mechanics priors, multiphase wellbore physics, and machine-learning inversion provides a practical and scalable route to safe and efficient drilling in complex HTHP environments.

CRediT authorship contribution statement

Cheng-Kai Weng: Writing – review & editing, Writing – original draft, Methodology, Investigation, Conceptualization. **Hong-Wei Yang:** Funding acquisition, Conceptualization. **Jun Li:** Supervision, Funding acquisition, Conceptualization. **Xian-Jun Chen:** Visualization, Methodology. **Gong-Hui Liu:** Supervision, Conceptualization. **Shu-Sheng Guo:** Visualization, Methodology. **Zhen-Yu Long:** Formal analysis. **Wang Chen:** Formal analysis.

Data availability

The data that has been used is confidential.

Declaration of competing interest

The authors declare that they have no known competing financial interests or personal relationships that could have appeared to influence the work reported in this paper.

Acknowledgments

This work was financially supported by the National Key R&D Program of China (No. 2023YFC3009200); the Major Scientific Research Instrument Development Program of National Natural Science Foundation of China (No. 52227804); the Joint Foundation Program of National Natural Science Foundation of China (No. U22B2072), the National Natural Science Foundation of China General Program (No. 52474018), the Science Foundation of China University of Petroleum, Beijing (No. 2462023BJRC008).

References

Caicedo, H.U., Calhoun, W.M., Ewy, R.T., 2005. Unique ROP predictor using bit-specific coefficient of sliding friction and mechanical efficiency as a function of confined compressive strength impacts drilling performance. In: SPE/IADC Drilling Conference. https://doi.org/10.2118/92576-MS.

Carneiro, T.C., Rocha, P.A.C., Carvalho, P.C.M., Fernández-Ramírez, L.M., 2022. Ridge regression ensemble of machine learning models applied to solar and wind forecasting in Brazil and Spain. Appl. Energy 314, 118936. https://doi.org/10.1016/j.apenergy.2022.118936.

Chen, X., Fan, H., Guo, B., et al., 2014. Real-time prediction and optimization of drilling performance based on a new mechanical specific energy model. Arabian J. Sci. Eng. 39, 8221–8231. https://doi.org/10.1007/s13369-014-1376-0.

Chen, X., Guo, S., Wang, S., et al., 2024. Application of new method for formation pressure monitoring of drilling machinery energy efficiency in Yingqiong Basin, South China Sea. Journal of China University of Petroleum (Edition of Natural Science) 48 (3), 188–197. https://doi.org/10.3969/j.issn.1673-5005.2024.03.021 (in Chinese).

Chen, X., Weng, C., Tao, L., et al., 2025. A novel method for predicting formation pore pressure ahead of the drill bit by embedding petrophysical theory into machine learning based on seismic and logging-while-drilling data. Pet. Sci. 22 (7), 2868–2883. https://doi.org/10.1016/j.petsci.2025.04.012.

Dabiri, M.S., Haji-Hashemi, R., Ashoorian, S., Schaffie, M., Zabihi, R., Hemmati-Sarapardeh, A.H., 2025. Modeling drilling fluid density at high-pressure high-temperature conditions using advanced machine-learning techniques. Geoenergy Sci. Eng. 244, 213369. https://doi.org/10.1016/j.geoen.2024.213369.

Dupriest, F.E., Koederitz, W.L., 2005. Maximizing drill rates with real-time surveillance of mechanical specific energy. In: SPE/IADC Drilling Conference. https://doi.org/10.2118/92194-MS.

Ehsan, M., Manzoor, U., Chen, R., et al., 2025. Pore pressure prediction based on conventional well logs and seismic data using an advanced machine learning approach. J. Rock Mech. Geotech. Eng. 17 (5), 2727–2740. https://doi.org/10.1016/j.jrmge.2024.09.049.

Erivwo, O., Makis, V., 2021. Improved abnormal formation pressure detection from drilling performance data in a partially observable setting. J. Petrol. Sci. Eng. 206, 108947. https://doi.org/10.1016/j.petrol.2021.108947.

Fan, C., Cao, J., Luo, J., et al., 2021. Heterogeneity and influencing factors of marine gravity flow tight sandstone under abnormally high pressure: A case study from the Miocene Huangliu Formation reservoirs in LD10 area, Yinggehai Basin, South China Sea. Petrol. Explor. Dev. 48 (5), 1048–1062. https://doi.org/10.1016/S1876-3804(21)60090-3.

Guo, S., Chen, X., Liao, G., et al., 2022. A quantitative evaluation method for predicting polygenetic overpressure in Yinggehai Basin. Journal of China University of Petroleum (Edition of Natural Science) 46 (6), 143–148. https://doi.org/10.3969/j.issn.1673-5005.2022.06.016 (in Chinese).

He, M., 2016. Influx real-time Interpretation theory and control method in managed pressure drilling. Ph.D Thesis. China University of Petroleum (Beijing), Beijing, China (in Chinese).

Holmes, C.S., Swift, S.C., 1970. Calculation of circulating mud temperatures. J. Petrol. Technol. 22, 670–674. https://doi.org/10.2118/2318-PA.

Hossain, M.E., Al-Majed, A.A., 2015. Fundamentals of Sustainable Drilling Engineering. John Wiley & Sons, Hoboken, NJ, USA.

Hottmann, C.E., Johnson, R.K., 1965. Estimation of formation pressures from log-derived shale properties. J. Petrol. Technol. 17 (6), 717–722. https://doi.org/10.2118/1110-PA.

Jorden, J.R., Shirley, O.J., 1966. Application of drilling performance data to overpressure detection. J. Petrol. Technol. 18 (11), 1387–1394. https://doi.org/10.2118/1407-PA.

Li, Z., Zhang, Z., Yang, J., et al., 2019. Research and application of formation pressure monitoring while drilling in deepwater with high temperature and high pressure. Earth Sci. 44 (8), 2597–2602. https://doi.org/10.3799/dqkx.2019.049 (in Chinese).

Liu, W., Deng, H., Zhu, X., et al., 2023. Experimental study of the rock cutting mechanism with PDC cutter under confining pressure condition. Rock Mech. Rock Eng. 56, 7377–7396. https://doi.org/10.1007/s00603-023-03444-7.

Long, Z., Li, J., Yang, H., et al., 2024. Methods and experiments for automatic control of surface back pressure based on dung beetle optimizer-PID controller. Process Saf. Environ. Prot. 191 (Part A), 360–374. https://doi.org/10.1016/j.psep.2024.08.121.

Majidi, R., Albertin, M., Last, N., 2017. Pore-pressure estimation by use of mechanical specific energy and drilling efficiency. SPE Drill. Complet. 32, 97–104. https://doi.org/10.2118/178842-PA.

Oloruntobi, O., Adedigba, S., Khan, F., et al., 2018. Overpressure prediction using the hydro-rotary specific energy concept. J. Nat. Gas Sci. Eng. 55, 243–253. https://doi.org/10.1016/j.jngse.2018.05.003.

Pennebaker, E.S., 1968. Detection of abnormal-pressure formation from seismic field data. Drilling and Production Practice. American Petroleum Institute, pp. 184–191.

Qin, J., Pang, X., Santra, A., et al., 2023. Various admixtures to mitigate the long-term strength retrogression of Portland cement cured under high pressure and high temperature conditions. J. Rock Mech. Geotech. Eng. 15 (1), 191–203. https://doi.org/10.1016/j.jrmge.2022.02.005.

Radwan, A.E., Wood, D.A., Radwan, A.A., 2022. Machine learning and data-driven prediction of pore pressure from geophysical logs: A case study for the Mangahewa gas field, New Zealand. J. Rock Mech. Geotech. Eng. 14 (6), 1799–1809. https://doi.org/10.1016/j.jrmge.2022.01.012.

Rashidi, M., Asadi, A., 2018. An artificial intelligence approach in estimation of formation pore pressure by critical drilling data. In: 52nd U.S. Rock Mechanics/Geomechanics Symposium.

Rehm, B., McClendon, R., 1971. Measurement of formation pressure from drilling data. In: Fall Meeting of the Society of Petroleum Engineers of AIME. https://doi.org/10.2118/3601-MS.

Rivas Cardona, J., 2011. Fundamental investigation of pore pressure prediction during drilling from the mechanical behavior of rock. Ph.D Thesis. Texas A&M University, Texas, USA.

Solano, Y.P., Uribe, R., Frydman, M., et al., 2007. A modified approach to predict pore pressure using the d exponent method: An example from the Carbonera formation, Colombia. CT&F-Cienc. Tecnol. Futuro 3 (3), 103–112.

Shajari, M., 2013. A modified approach to predict pore pressure using the d exponent method: An example from an oil field, south of Iran. Petrol. Sci. Technol. 31 (10), 1008–1017. https://doi.org/10.1080/10916466.2010.531350.

Teale, R., 1965. The concept of specific energy in rock drilling. Int. J. Rock Mech. Min. Sci. Geomech. Abstr. 2 (1), 57–73. https://doi.org/10.1016/0148-9062(65)90022-7.

Wang, B., Li, J., Zhang, G., et al., 2023. A novel early gas kick monitoring method using the difference between downhole dual measurement points pressure and a genetic algorithm-based model. Geoenergy Sci. Eng. 231 (Part A), 212371. https://doi.org/10.1016/j.geoen.2023.212371.

Yang, H., Feng, Y., Shang, G., et al., 2025. A sequence learning approach for real-time and ahead-of-bit pore pressure prediction utilizing drilling data from the drilled section. SPE J. 30, 524–543. https://doi.org/10.2118/223962-PA.

Yang, H., Li, J., Liu, G., et al., 2019. Numerical analysis of transient wellbore thermal behavior in dynamic deepwater multi-gradient drilling. Energy 179, 138–153. https://doi.org/10.1016/j.energy.2019.04.214.

Yang, H., Li, J., Zhang, H., et al., 2022. Thermal behavior prediction and adaptation analysis of a reelwell drilling method for closed-loop geothermal system. Appl. Energy 320, 119339. https://doi.org/10.1016/j.apenergy.2022.119339.

Yang, J., Li, G., Li, Q., 2005. Research of inspecting while drilling in high-temperature and high-pressure formation. Oil Drilling & Production Technology (3), 18–19. https://doi.org/10.13639/j.odpt.2005.03.008 (in Chinese).

Zhang, D., Ma, T., Liu, Y., et al., 2025. Heterogeneous multi-task learning approach for rock strength prediction in real-time during drilling based on mud log data. Geoenergy Sci. Eng. 246, 213608. https://doi.org/10.1016/j.geoen.2024.213608 (in Chinese).

Zhang, H., Pei, J., Zhang, Y., et al., 2013. Overpressure reservoirs of the Huangliu Formation of the Dongfang area, Yinggehai Basin, South China Sea. Petrol. Explor. Dev. 40 (3), 305–315. https://doi.org/10.1016/S1876-3804(13)60037-3.